when the body was insufficiently lifted. Additionally, when the tail was lifted clear of the media in robot experiments, the posterior motor and mounting structures intruded into and dragged through the media, resulting in an intrusion that was difficult to model; therefore, we simulated trials with the tail intruding into the media in the same configuration as at the end of tail-thrusting behavior, which yielded similar performance. To test these assumptions, we compared results to a subset of robot trials, and obtained good agreement between simulation and experiment (Fig. 4C and fig. S4).

The change in the patterns of the local connection vector fields revealed how limbs and tail could coordinate to produce movement (Fig. 4, C to E). For example, these fields demonstrated that the tail was not uniformly beneficial in all situations, nor even substantially beneficial in horizontal movement, in which the vertical component of the vectors (tail contribution) was small. However, as surface incline angle increased, the horizontal magnitudes of connection vectors decreased, indicating reduced efficacy of limb-only tail-dragging gaits (a horizontal path across the vector field). The relatively larger vertical component across more of the shape space indicated the increased importance of the tail to forward movement. The optimal gait for both inclines was close to the synchronous thrusting used by the robot and mudskipper, yielding similar displacements (Fig. 4, C to E); phase lag between initiation of limb and tail movement was suboptimal and, in one case per incline, yielded the worst possible gait (Fig. 4, D and E). Improper use of the tail resulted in substantially lower performance than simply allowing it to drag (Fig. 4, C to E). Additionally, the generally downward direction of the vectors in both fields demonstrate that purely tail-powered locomotion (a vertical path down the right of the vector field) can produce forward motion, as seen in some extant fish (*12*).

Our results from a biological analog of early tetrapods and robophysical and mathematical models demonstrate that the tail can play an important role in limb-driven crutching locomotion on inclined granular substrates by making locomotors more robust to suboptimal kinematics and substrate conditions. This suggests that the sizable, well-ossified (and presumably well-muscled) tails of early tetrapods (*15*–*17*), originally used for swimming, may have been co-opted to promote reliable locomotion over challenging substrates, providing an exaptation (*36*) that facilitated their invasion of land. Although evidence of tail use is absent among the few fossil trackways attributed to early tetrapods (*37*, *38*), tail use might be evident in trackways formed on inclined shores.

REFERENCES AND NOTES

1. J. A. Clack, *Gaining Ground: The Origin and Evolution of Tetrapods* (Indiana Univ. Press, 2002).
2. E. B. Daeschler, N. H. Shubin, F. A. Jenkins Jr., *Nature* **440**, 757–763 (2006).
3. A. Blieck *et al.*, *Geol. Soc. London Spec. Publ. 278*, 219–235 (2007).
4. N. Gravish, P. B. Umbanhowar, D. I. Goldman, *Phys. Rev. Lett.* **105**, 128301 (2010).
5. H. Marvi *et al.*, *Science* **346**, 224–229 (2014).
6. F. Qian *et al.*, *Bioinspir. Biomim.* **10**, 056014 (2015).
7. C. Li, P. B. Umbanhowar, H. Komsuoglu, D. E. Koditschek, D. I. Goldman, *Proc. Natl. Acad. Sci. U.S.A.* **106**, 3029–3034 (2009).
8. N. Mazouchova, P. B. Umbanhowar, D. I. Goldman, *Bioinspir. Biomim.* **8**, 026007 (2013).
9. J. Davenport, A. K. M. A. Matin, *J. Fish Biol.* **37**, 175–184 (1990).
10. A. G. Johnels, *Oikos* **8**, 122 (1957).
11. C. M. Pace, A. C. Gibb, *J. Exp. Biol.* **214**, 530–537 (2011).
12. C. M. Pace, A. C. Gibb, *J. Fish Biol.* **84**, 639–660 (2014).
13. A. Jusufi, D. I. Goldman, S. Revzen, R. J. Full, *Proc. Natl. Acad. Sci. U.S.A.* **105**, 4215–4219 (2008).
14. T. Libby *et al.*, *Nature* **481**, 181–184 (2012).
15. E. Jarvik, *Medd. Gronl.* **114**, 1–90 (1952).
16. E. Jarvik, *The Devonian Tetrapod* Ichthyostega (Indiana Univ. Press, 1996).
17. M. I. Coates, *Trans. R. Soc. Edinb. Earth Sci.* **87**, 363–421 (1996).
18. R. W. Blob, *Paleobiology* **27**, 14–38 (2001).
19. M. A. Ashley-Ross, S. T. Hsieh, A. C. Gibb, R. W. Blob, *Integr. Comp. Biol.* **53**, 192–196 (2013).
20. S. E. Pierce, J. A. Clack, J. R. Hutchinson, *Nature* **486**, 523–526 (2012).
21. S. E. Pierce, J. R. Hutchinson, J. A. Clack, *Integr. Comp. Biol.* **53**, 209–223 (2013).
22. E. M. Standen, T. Y. Du, H. C. E. Larsson, *Nature* **513**, 54–58 (2014).
23. S. M. Kawano, R. W. Blob, *Integr. Comp. Biol.* **53**, 283–294 (2013).
24. V. A. Harris, *Proc. Zool. Soc. London* **134**, 107–135 (1960).
25. B. O. Swanson, A. C. Gibb, *J. Exp. Biol.* **207**, 4037–4044 (2004).
26. J. Aguilar, D. I. Goldman, *Nat. Phys.* **12**, 278 (2016).
27. A. Shapere, F. Wilczek, *Phys. Rev. Lett.* **58**, 2051–2054 (1987).
28. R. L. Hatton, Y. Ding, H. Choset, D. I. Goldman, *Phys. Rev. Lett.* **110**, 078101 (2013).
29. N. Mitarai, F. Nori, *Adv. Phys.* **55**, 1–45 (2006).
30. S. S. Sharpe, R. Kuckuk, D. I. Goldman, *Phys. Biol.* **12**, 046009 (2015).
31. H. Askari, K. Kamrin, http://arxiv.org/abs/1510.02966 (2015).
32. K. Nishikawa *et al.*, *Integr. Comp. Biol.* **47**, 16–54 (2007).
33. C. Li, T. Zhang, D. I. Goldman, *Science* **339**, 1408–1412 (2013).
34. S. D. Kelly, R. M. Murray, *J. Robot. Syst.* **12**, 417–431 (1995).
35. R. D. Maladen, Y. Ding, C. Li, D. I. Goldman, *Science* **325**, 314–318 (2009).
36. S. J. Gould, E. S. Vrba, *Paleobiology* **8**, 4–15 (1982).
37. J. Clack, *Palaeogeogr. Palaeoclimatol. Palaeoecol.* **130**, 227–250 (1997).
38. S. Curth, M. S. Fischer, J. A. Nyakatura, *Ichnos* **21**, 32–43 (2014).

ACKNOWLEDGMENTS

Supported by NSF grants PoLS PHY-1205878, PHY-1150760, and CMMI-1361778, Army Research Office (ARO) grant W911NF-11-1-0514, and the ARL MAST CTA (D.I.G.); ARO Robotics CTA and NSF National Robotics Initiative IIS-1426655 (H.C.); NSF grants IOS-0517340 and IOS-0817794 (R.W.B.); GT UROP and the GT PURA Travel Grant (B.M.); a Clemson University Wade Stackhouse Fellowship, NSF award DBI-1300426, and the University of Tennessee, Knoxville (S.M.K.); and the U.S. Department of Defense, Air Force Office of Scientific Research, National Defense Science and Engineering Graduate (NDSEG) Fellowship, 32 CFR 168a (P.E.S.). The authors declare no conflicts of interest. Data are available from the corresponding author upon request.

SUPPLEMENTARY MATERIALS

www.sciencemag.org/content/353/6295/154/suppl/DC1
Materials and Methods
Supplementary Text
Figs. S1 to S6
Table S1
Movies S1 to S6
References (*39*, *40*)

16 December 2015; accepted 26 May 2016
10.1126/science.aaf0984

ROBOTICS

Phototactic guidance of a tissue-engineered soft-robotic ray

Sung-Jin Park,[1] Mattia Gazzola,[2]* Kyung Soo Park,[3,4]† Shirley Park,[5]‡ Valentina Di Santo,[6] Erin L. Blevins,[6]§ Johan U. Lind,[1] Patrick H. Campbell,[1] Stephanie Dauth,[1] Andrew K. Capulli,[1] Francesco S. Pasqualini,[1] Seungkuk Ahn,[1] Alexander Cho,[1] Hongyan Yuan,[1]|| Ben M. Maoz,[1] Ragu Vijaykumar,[5] Jeong-Woo Choi,[3,4] Karl Deisseroth,[5,7] George V. Lauder,[6] L. Mahadevan,[2,8] Kevin Kit Parker[1,4]¶

Inspired by the relatively simple morphological blueprint provided by batoid fish such as stingrays and skates, we created a biohybrid system that enables an artificial animal—a tissue-engineered ray—to swim and phototactically follow a light cue. By patterning dissociated rat cardiomyocytes on an elastomeric body enclosing a microfabricated gold skeleton, we replicated fish morphology at $^{1}/_{10}$ scale and captured basic fin deflection patterns of batoid fish. Optogenetics allows for phototactic guidance, steering, and turning maneuvers. Optical stimulation induced sequential muscle activation via serpentine-patterned muscle circuits, leading to coordinated undulatory swimming. The speed and direction of the ray was controlled by modulating light frequency and by independently eliciting right and left fins, allowing the biohybrid machine to maneuver through an obstacle course.

Bioinspired design, as applied to robotics, aims at implementing naturally occurring features such as soft materials, morphologies, gaits, and control mechanisms in artificial settings in order to improve performance (*1*–*4*). For example, recent soft-robotics studies raised awareness on the importance of material properties (*3*, *4*), shifting the focus from rigid elements to soft materials, whereas other investigations report successful mimicry of gaits or morphological features inspired by insects (*5*, *6*), fish (*7*, *8*), snakes (*9*), salamanders (*10*), and cheetahs (*11*). Although recent advances have the promise of bridging the performance gap with animals,

the current soft-robotic actuators based on, for instance, electroactive polymers, shape memory alloys, or pressurized fluids are yet to mature to the point of replicating the high-resolution complex movements of biological muscles (*3*, *4*).

In this context, biosensors and bioactuators (*12*) are intriguing alternatives because they can intrinsically respond to a number of control inputs (such as electric fields and optical stimulation). Thanks to recent advances in genetic tools (*13*) and tissue engineering (*12*), these responses can be altered and tuned across a wide range of time and length scales. Some pioneering studies have exploited these technologies for self-propulsion, developing miniaturized walking machines (*14*–*16*) and flagellar (*17*) or jellyfish-inspired (*18*) swimming devices. These biohybrid systems operate at high energy efficiency and harvest power from energy-dense, locally available nutrients, although at present they require specialized environments (physiological solutions) that may limit their applicability. Moreover, these biohybrid locomotors lack the reflexive control (*9*, *19*) necessary to enable adaptive maneuvering and thus the ability to respond to spatiotemporally varying external stimuli.

We designed, built, and tested a tissue-engineered analog of a batoid fish such as stingrays and skates. By combining soft materials and tissue engineering with optogenetics, we created an integrated sensory-motor system that allowed for coordinated undulating fin movement and phototactically controlled locomotion that is guided via light stimuli. We drew from fish morphology, neuromuscular dynamics, and gait control to implement a living, biohybrid system that leads to robust and reproducible locomotion and turning maneuvers. Batoid fish are ideal biological models in robotics (*8*) because their nearly planar bauplan is characterized by a broad dorsoventral disk, with a flattened body and extended pectoral fins, that enhances stability against roll (*20*). They swim with high energy efficiency (*21*) by generating spanwise bending deformations and chordwise front-to-rear undulatory motion (Fig. 1A and movie S1) (*20*, *22*) via the sequential activation of pectoral fin muscles. This undulatory gait allows slender aquatic animals to channel body movement into forward motion by exchanging momentum with the fluid (*7*, *22*) and is a convergent mode of aquatic propulsion (*23*). Moreover, batoids can use these undulatory modes for fine maneuvering and turning by independently and asymmetrically actuating their pectoral fins (*24*). Inspired by batoids, we reverse-engineered their musculoskeletal structure (Fig. 1B and fig. S1) via a four-layered architecture (Fig. 1C): a three-dimensional elastomer [polydimethylsiloxane (PDMS)] body, cast via a titanium mold (fig. S2A and movie S2); a chemically neutral skeleton fabricated by means of thermal evaporation of gold through a custom designed shadow mask; a thin interstitial elastomer layer obtained by spin-coating; and last, a layer of aligned rat cardiomyocytes generated via microcontact printing of fibronectin (fig. S3) (*25*).

This design yielded a tissue-engineered ray with a single muscle layer capable of downward contraction (Fig. 1, C and D). Upward contraction would require a second layer of muscle that acts antagonistically to the upper layer. To minimize the complexity of our design, we instead used an asymmetrical stiff gold skeleton that stores elastic energy during the downstroke and rebounds during the subsequent relaxation phase. Inspired by histological analysis (fig. S1) as well as theoretical considerations (*26*), we channeled muscular work and elastic energy into forward motion by breaking fore-aft symmetry through a varying body rigidity along the anterior-posterior axis. This was achieved via a thicker body and a denser and radially further reaching skeleton pattern in the front (Figs. 1, C and D, and 2A and fig. S2A). Likewise, along the proximal-distal axis, flexibility of the fins was enhanced by gradually reducing their thickness (fig. S2A). Last, the PDMS mixture was adjusted (*25*) to provide body rigidity and fin flexibility while conserving overall neutral buoyancy (fig. S2).

The composite supporting structure described above was coupled to a tissue-engineered muscle layer, which captured the salient musculoskeletal features of batoid fish (Fig. 2B). At the mesoscale (50 μm to 5 mm), batoid myofibers are tightly bundled and are aligned in the radial direction parallel to the rays of the skeleton (Fig. 2B). At the microscale (1 to 10 μm), the Z-lines of the sarcomeres (the cell force–generating units) (Fig. 2C) present strong nematic alignment perpendicular to individual myofibers so as to focus contraction forces. Following this layout, the muscles and sarcomeres of the tissue-engineered ray were designed to orient radially from the body and parallel to the gold skeleton rays (Fig. 2B and fig. S4), and the Z-lines of the sarcomeres were engineered to be perpendicular to the skeleton rays through microscale patterning of fibronectin (Fig. 2C and fig. S4).

Last, to mimic the sensory-somatic nervous system that controls the sequential activation of fin muscles in the batoid fish, we recast the neurocontrol problem as a design problem. A possible solution is given by serpentine-patterned muscle circuits that physically determine the propagation of muscle contraction in space and time (Figs. 1D and 2, D and E), leading to hardwired coordination that could be triggered with external

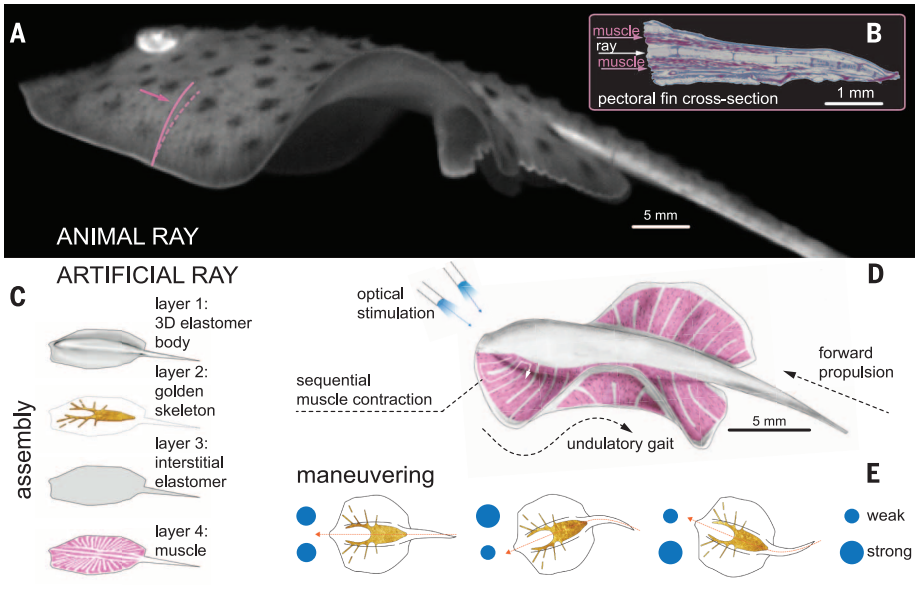

Fig. 1. Bioinspired concept design of the tissue-engineered ray. (**A**) A live Little skate, *Leucoraja erinacea*, swimming and (**B**) its musculoskeletal structure. (**C** to **E**) Tissue-engineered ray with (C) four layers of body architecture, (D) concept, and (E) phototactic control. Upon optical stimulation, the tissue-engineered ray induces sequential muscle activation via serpentine-patterned muscle tissues, generates undulatory locomotion, and sustains steady forward swimming. It changes direction by generating asymmetric undulating motion between left and right fins, modulated by light pulse frequency.

[1]Disease Biophysics Group, Wyss Institute for Biologically Inspired Engineering, John A. Paulson School of Engineering and Applied Sciences, Harvard University, Cambridge, MA 02138, USA. [2]John A. Paulson School of Engineering and Applied Sciences, Harvard University, Cambridge, MA 02138, USA. [3]Department of Chemical and Biomolecular Engineering, Sogang University, Seoul 121-742, Korea. [4]Sogang-Harvard Research Center for Disease Biophysics, Sogang University, Seoul 121-742, Korea. [5]Department of Bioengineering, Stanford University, Stanford, CA 94305, USA. [6]Museum of Comparative Zoology, Harvard University, Cambridge, MA 02138, USA. [7]Department of Psychiatry and Behavioral Sciences and the Howard Hughes Medical Institute, Stanford University, Stanford, CA 94305, USA. [8]Department of Organismic and Evolutionary Biology, Department of Physics, Wyss Institute for Biologically Inspired Engineering, Kavli Institute for Nanobio Science and Technology, Harvard University, Cambridge, MA 02138S, USA.
*Present address: Department of Mechanical Science and Engineering, University of Illinois at Urbana-Champaign, Urbana, IL 61801, USA. †Present address: Department of Biomedical Engineering, University of Michigan, Ann Arbor, MI 48109, USA. ‡Present address: Department of Cardiovascular Medicine, Stanford University Medical Center, Stanford, CA 94305, USA. §Present address: The Winsor School, Boston, MA 02215, USA. ||Present address: Department of Mechanical, Industrial and Systems Engineering, University of Rhode Island, Kingston, RI 02881, USA.
¶Corresponding author. Email: kkparker@seas.harvard.edu

stimuli. This design was implemented by overlaying onto anisotropic tissue a layer of cardiomyocytes that were electrically coupled with gap junctions (fig. S4H). These myocytes were engineered to respond to optical stimuli (Fig. 1D) by expressing a light-sensitive ion channel [channelrhodopsin-2 (ChR2)] (*27*). Thus, a point light stimulus directed at the front of the ray triggers the propagation of an action potential that is spatially and temporally modulated by the gap junctions between muscle cells without the need for neural coupling and coordination (Fig. 2, D and E). The expression of ChR2 was obtained via lentiviral transduction mediated by the truncated cardiac troponin T promoter cTnT (fig. S5) (*25*, *28*). This approach led to an 88% transduction rate of cardiomyocytes and maximized the sensitivity to blue light at powers of ~10 mW (fig. S5).

Optical stimulation of the circuits initiated sequential activation waves that propagated along the anterior-posterior axis as revealed by means of calcium imaging (*25*) for three different circuit designs (Fig. 2D, fig. S6, and movies S3 and S4). Dense serpentine patterns enhanced activation localization, whereas rarefied ones increased propagation speed (figs. S7 and S8). To allow for maneuverability, we ensured that each pectoral fin could be independently actuated by pacing left and right optical stimuli at different frequencies (fig. S6 and movie S5). Among the various designs considered, the circuit of choice was characterized by the intermediate serpentine pattern density (Fig. 2E). This circuit represented the best tradeoff between overlap with batoids' operating range and contraction time reproducibility (low standard error) in order to minimize desynchronization and undesired turning (Fig. 2E). The final overall design of our ray consists of ~200,000 live cardiomyocytes in an elastomeric body of 16.3 mm length and 10.18 ± 0.43 mg mass.

When immersed in a 37°C Tyrode's physiological salt solution containing glucose as energy reservoir, and upon optical stimulation, the fabricated ray was propelled by producing forward thrust via the undulatory motion of its fins (Fig. 3 and movie S6). Video-tracking analysis (*25*) showed that during each swimming cycle, as the calcium signal propagated (fig. S9), the anterior region bent downward, while the posterior one lifted upward (Fig. 3, A and B), conferring a small downward orientation (–10°) to the ray's longitudinal axis (fig. S9). Both regions reached their maximum displacement around ~200 ms (Fig. 3B), when their motion gradually inverted until ~340 ms

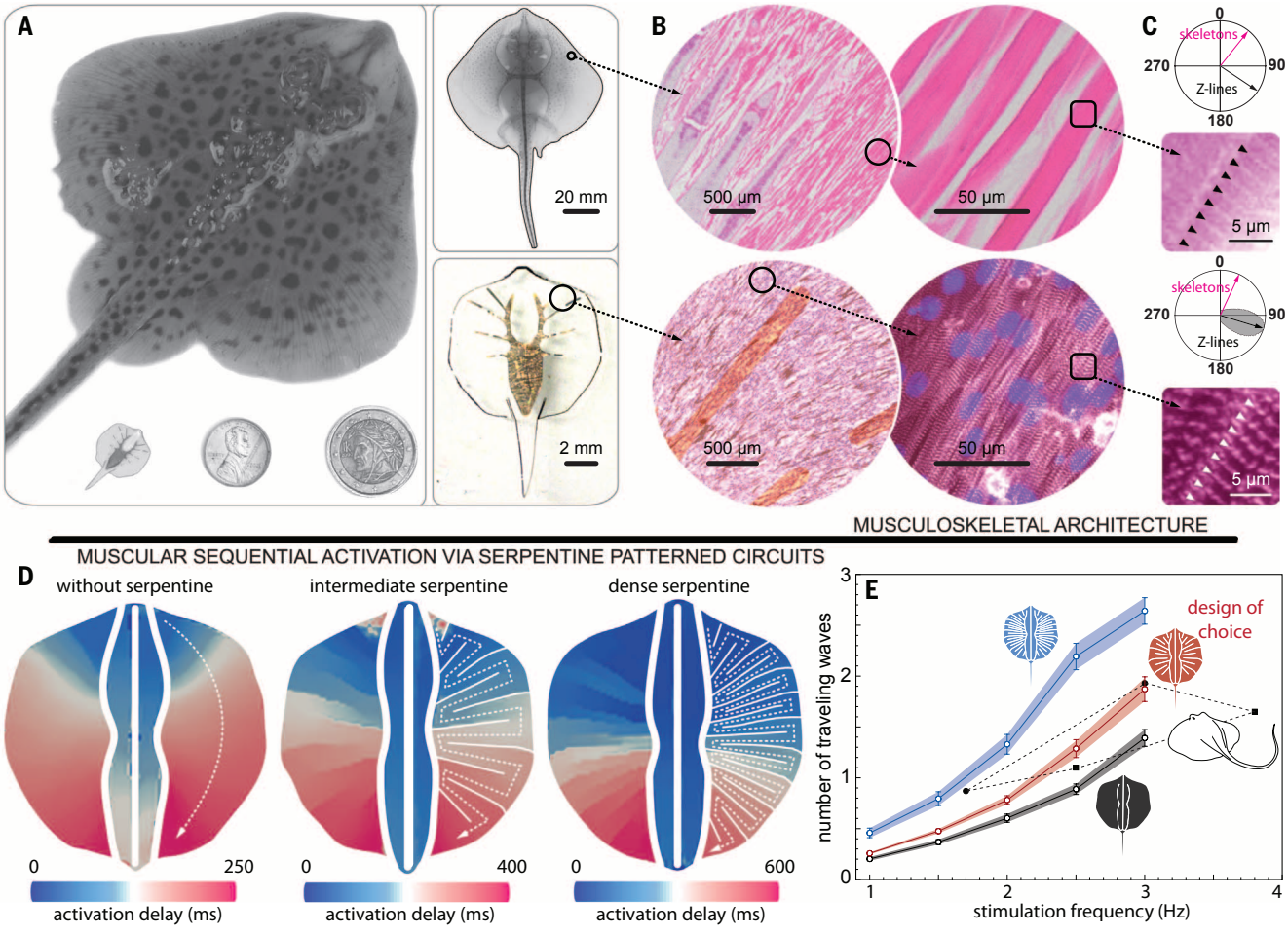

Fig. 2. Engineering solutions. (**A**) System-level design for skate (top) and tissue-engineered ray (bottom left) comparable with one penny and a two Euros coin (bottom middle and right). (**B** and **C**) Musculoskeletal (B) meso- and (C) micro-architecture of a skate, *L. erinacea* (top), is replicated in a tissue-engineered ray (bottom). Horizontal sections of the skate were stained with hematoxylin and eosin (top), and the engineered tissue was immunostained with a light-sensitive membrane protein, ChR2 (red, bottom left), sarcomeric α-actinin [red, (B), bottom right, and (C)], and nuclei (blue, (B), bottom right). (C) Orientation of the Z-lines (skate, black arrow and black triangles, top; and tissue-engineered ray, black arrow with gray distribution and white triangles, bottom). In both cases, Z-lines are perpendicular to the skeleton rays (pink arrows). (**D**) Muscle circuits with preprogrammed activation pattern. A point light stimulus directed at the front of the fins with 1.5 Hz frequency triggers the calcium wave that propagates along the predefined serpentine patterns. (**E**) Operating range of the muscle circuits. The circuit with intermediate serpentine pattern density represents the best tradeoff between contraction time reproducibility (SEM) and overlap with batoids' operating range [*Taeniura lymma* (*20*) and *Potamotrygon orbignyi* (*22*), black symbols]. Black, red, and blue indicates muscle circuit without serpentine patterns and with intermediate and dense serpentine patterns, respectively. Each colored band indicates SEM of number of traveling waves.

(Fig. 3, C and D). At this point, the calcium wave had traveled ~70% of the ray body and approached the flexible tail region (Fig. 3E and fig. S9). This signal caused a rapid, strong downward contraction of the rear of the body, a quick upward recoil of the head region (presumably mediated by the stiff skeleton) (Fig. 3), a 30° upward reorientation of the longitudinal axis (fig. S9), and a spike in forward swimming speed (Fig. 3E). After 340 ms, the calcium wave vanishes, and the ray relaxes (Fig. 3E and fig. S9), gliding until its forward momentum dissipates.

A periodical optical stimulation leads to a rhythmically sustained forward displacement (Fig. 3F). To test the benefits of spatiotemporally modulated undulatory locomotion relative to pulsatile locomotion (typical of jellyfish), we stimulated our design of choice via a global electrical field (*25*). The latter, unlike optical point stimulation, induces a global, synchronized contraction of the entire muscle layer, leading to jet-like propulsion (movie S7). Although pulsatile actuation also produced forward motion, undulatory gaits were found to be twice as fast at 1.5 Hz pacing (Fig. 3G).

We compared the kinematics (Fig. 3, H and I) and hydrodynamics (Fig. 3, J to M) of bioinspired and live rays. Both rays exhibit asymmetric deformation patterns in which the deflection amplitude progressively increases in the radially outward and anterior-posterior directions. This similarity shows that our asymmetric composite structure compensates for the lack of the upper muscle layer (Fig. 3, B and D), leading to the coordinated undulatory locomotion. Our design of choice was found to outperform a symmetric design (by 5.7×, as measured by distance traveled per unit time) as well as asymmetric designs without gold skeleton (2.7×), with denser gold skeleton (8.2×), and with thinner (1.5×) and thicker fins (3.3×) (fig. S10 and movie S8 and S9). Particle image velocimetry (PIV) (*25*) images of the hydrodynamic footprint of the tissue-engineered ray (Fig. 3, A to D) show that body contractions generate vortices of alternating sign that are sequentially shed downstream in the wake (Fig. 3, A to D, and movie S10), which is the hallmark of inertial undulatory swimming (*29*). Indeed, PIV of live skates (Fig. 3, K to M, and fig. S11) reveals a qualitatively similar alternation of positive and negative vortices, respectively generated in concave and convex regions of the body.

We emphasize here that our ray is a 10-fold scaled-down version of a live skate and moves in a laminar flow regime, as opposed to batoid fish that operate in turbulent conditions. Thus, a direct performance comparison is not meaningful, but it is instructive to contextualize artificial and natural solutions in terms of a recent scaling framework (*23*, *30*). All inertial undulatory swimmers hew to two scaling laws, $Re = Sw^{4/3}$ in the laminar regime and $Re = Sw$ in the turbulent regime, where the Swimming number $Sw = 2\pi fAL/\upsilon$ (L is the characteristic length of the swimmer, f is the undulation frequency, A is the amplitude, and υ is the fluid viscosity) captures input kinematics, and the Reynolds number $Re = UL/\upsilon$ (where U is the forward speed) captures output speed. By fitting extant biological data (*23*), the average swimming "roofline" was determined, thus providing an objective way to assess swimming performance. In this analysis, our tissue-engineered rays reached up to 63% of the Re of comparable natural solutions at the given Sw (Fig. 3J).

For gait control, we first determined a set of gait protocols for speed and direction control by modulating light frequency and by synchronously or asynchronously triggering the right and left serpentine circuits (figs. S11 and S12 and movies S12 to S18). Synchronous pacing on both fins resulted in straight, forward displacement (figs. S11 and S12 and movies S12 and S13), whereas stimulation frequency determined the swimming speed range (maximum at 1.5 to 2 Hz, minimum at 1 or 3 Hz) (fig. S10E and movies S14 to S16). Asynchronous pacing instead resulted in directional

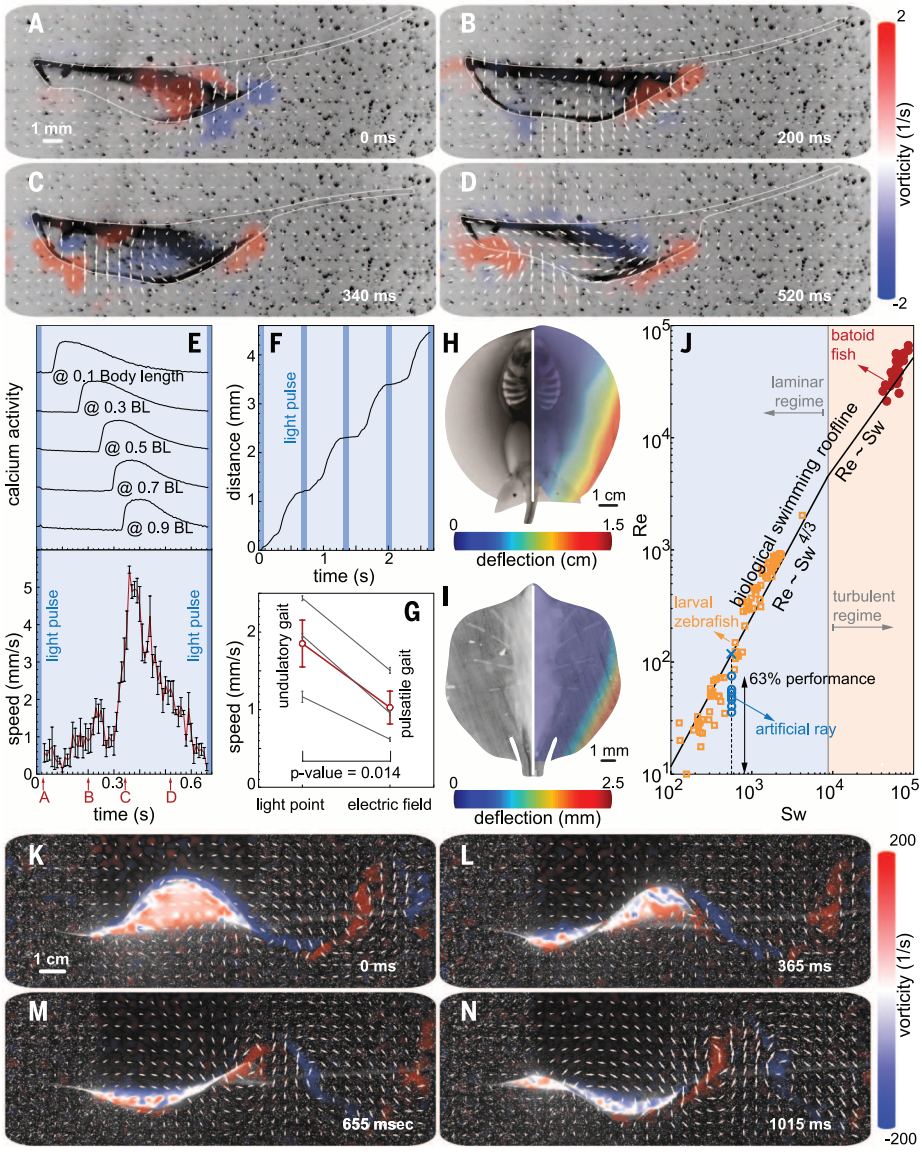

Fig. 3. Kinematics and hydrodynamics. (**A** to **D**) PIV flow measurements highlight the production of alternated positive and negative vortices by the tissue-engineered ray. The viscosity associated with the relatively small *Re* is responsible for the dissipation of the vortex street in the wake. (**E**) Correlation between calcium activity and undulatory locomotion. (**F**) The moving distance during four strokes. (**G**) Comparison of swimming speed between the tissue-engineered rays stimulated by point and field stimulations. Undulatory locomotion produced by sequential muscle activation (point, 1.85 mm/s) improved swimming speed significantly compared with pulsatile propulsion generated by global muscle activation (field, 1.03 mm/s; matched pairs test, $P = 0.014$, $n = 3$ rays). Gray and red lines indicate the speed of individual rays and their average, respectively. (**H** and **I**) Out-of-plane fin deflection in both (H) a live stingray, *P. orbignyi*, and (I) a tissue-engineered ray (maximum amplitude, 2.54 ± 0.02 mm). (**J**) Comparison of swimming performance between tissue-engineered rays ($n = 7$ rays) and aquatic swimmers [batoid fish (*20*) and larval zebrafish (*32*)] following the scaling analysis (*23*). [Figure adapted from (*23*).] (**K** to **N**) PIV analysis of live Little skate, *L. erinacea*.

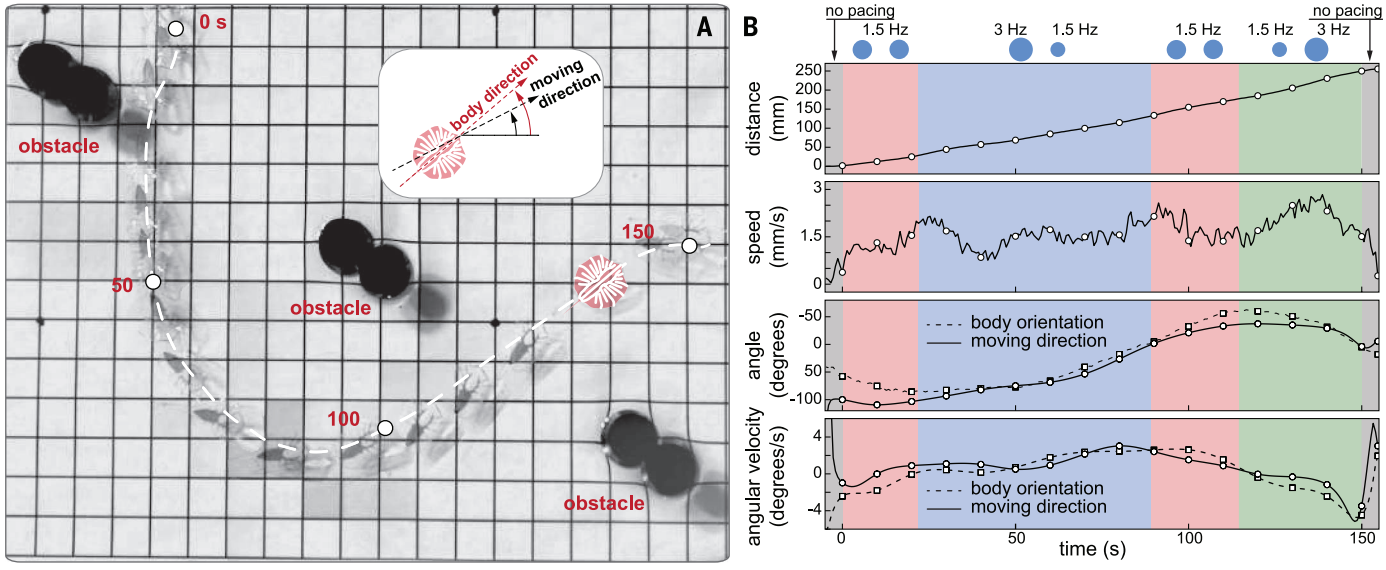

Fig. 4. Phototactic steering of the tissue-engineered ray through an obstacle course. (**A**) The ray completed a course that required complex coordination and maneuvering. Motion began with a forward protocol (at 0 s) to gain acceleration. A following left turn protocol allowed the ray to overcome forward momentum, making a left turn (at ~50 s). Next, another forward protocol was used to dissipate counterclockwise angular momentum and regain directionality (at ~100 s). While the ray made its way back to the other side of the obstacles, a final right turn protocol was given to make a right turn, winding the last obstacle. Grids, 1 cm. (**B**) Corresponding kinematic analysis relative to light frequency modulation protocols used for guidance.

turns (fig. S12, B, C, and F). In order to minimize the turning radius, we paired stimulation frequencies (1/1.5 Hz in movie S17, or 3/1.5 Hz in movie S18) to maximize the actuation difference between fins. Our ray turned in either clockwise or counterclockwise directions by generating asymmetric undulating motion between left and right fins, as in batoid fishes (*24*).

Last, we challenged the tissue-engineered ray to swim through an obstacle course. Using the above gait and turning protocols, we guided the ray along a curved path by alternating forward motion and turning maneuvers, at an average speed of ~1.5 mm/s over a distance of ~250 mm, 15 times longer than its body length (Fig. 4 and movie S19). Furthermore, the ray was found able to maintain 80% of its initial speed for up to 6 consecutive days (fig. S13 and movie S20). Therefore, our ray outperformed existing locomotive biohybrid systems in terms of speed [3.2 mm/s in movie S16, 1.3× over jellyfish (*18*)], distance traveled [~250 mm, 35× over cantilever-like walkers (*15*)], and durability (6 days), demonstrating the potential of self-propelled, phototactically activated tissue-engineered robots.

With dissociated cells, naturally equipped with biosensors and bioactuators, as a programmable, actuating building material, we used optogenetics and tissue engineering to build an adaptive swimming animal. Our study is but a first step in engineering multilevel systems that link neurodynamics, mechanics, and complex controllable gaits—coupling sensory information to motor coordination and movement that leads to behavior. This work paves the way for the development of autonomous and adaptive artificial creatures able to process multiple sensory inputs and produce complex behaviors in distributed systems and may represent a path toward soft-robotic "embodied cognition" (*4*, *31*).

REFERENCES AND NOTES

1. R. Pfeifer, M. Lungarella, F. Iida, *Science* **318**, 1088–1093 (2007).
2. M. Haberland, S. Kim, *Bioinspir. Biomim.* **10**, 016010 (2015).
3. S. Kim, C. Laschi, B. Trimmer, *Trends Biotechnol.* **31**, 287–294 (2013).
4. D. Rus, M. T. Tolley, *Nature* **521**, 467–475 (2015).
5. K. Y. Ma, P. Chirarattananon, S. B. Fuller, R. J. Wood, *Science* **340**, 603–607 (2013).
6. J. S. Koh *et al.*, *Science* **349**, 517–521 (2015).
7. M. S. Triantafyllou, G. S. Triantafyllou, *Sci. Am.* **272**, 64–70 (1995).
8. K. W. Moored, F. E. Fish, T. H. Kemp, H. Bart-Smith, *Mar. Technol. Soc. J.* **45**, 99–109 (2011).
9. H. C. Astley *et al.*, *Proc. Natl. Acad. Sci. U.S.A.* **112**, 6200–6205 (2015).
10. A. J. Ijspeert, A. Crespi, D. Ryczko, J. M. Cabelguen, *Science* **315**, 1416–1420 (2007).
11. D. J. Hyun, S. Seok, J. Lee, S. Kim, *Int. J. Robot. Res.* **33**, 1417–1445 (2014).
12. V. Chan, H. H. Asada, R. Bashir, *Lab Chip* **14**, 653–670 (2014).
13. J. D. Sander, J. K. Joung, *Nat. Biotechnol.* **32**, 347–355 (2014).
14. A. W. Feinberg *et al.*, *Science* **317**, 1366–1370 (2007).
15. V. Chan *et al.*, *Sci Rep* **2**, 857 (2012).
16. R. Raman *et al.*, *Proc. Natl. Acad. Sci. U.S.A.* **113**, 3497–3502 (2016).
17. B. J. Williams, S. V. Anand, J. Rajagopalan, M. T. A. Saif, *Nat. Commun.* **5**, 3081 (2014).
18. J. C. Nawroth *et al.*, *Nat. Biotechnol.* **30**, 792–797 (2012).
19. V. Braitenberg, *Vehicles: Experiments in Synthetic Psychology* (MIT Press, 1986).
20. L. J. Rosenberger, M. W. Westneat, *J. Exp. Biol.* **202**, 3523–3539 (1999).
21. V. Di Santo, C. P. Kenaley, *J. Exp. Biol.* **219**, 1804–1807 (2016).
22. E. L. Blevins, G. V. Lauder, *J. Exp. Biol.* **215**, 3231–3241 (2012).
23. M. Gazzola, M. Argentina, L. Mahadevan, *Nat. Phys.* **10**, 758–761 (2014).
24. J. M. Parson, F. E. Fish, A. J. Nicastro, *J. Exp. Mar. Biol. Ecol.* **402**, 12–18 (2011).
25. Materials and methods are available as supplementary materials on *Science* Online.
26. M. Gazzola, M. Argentina, L. Mahadevan, *Proc. Natl. Acad. Sci. U.S.A.* **112**, 3874–3879 (2015).
27. E. S. Boyden, F. Zhang, E. Bamberg, G. Nagel, K. Deisseroth, *Nat. Neurosci.* **8**, 1263–1268 (2005).
28. H. Ma, C. M. Sumbilla, I. K. G. Farrance, M. G. Klein, G. Inesi, *Am. J. Physiol. Cell Physiol.* **286**, C556–C564 (2004).
29. W. M. van Rees, M. Gazzola, P. Koumoutsakos, *J. Fluid Mech.* **722**, R3 (2013).
30. A. J. Cote, P. W. Webb, *Integr. Comp. Biol.* **55**, 662–672 (2015).
31. R. Pfeifer, H. G. Marques, F. Iida, Soft robotics: The next generation of intelligent machines. *Proceedings of the Twenty-Third International Joint Conference on Artificial Intelligence*, 3–9 August 2013, Beijing, China, pp. 5–11 (2013).
32. U. K. Müller, J. L. van Leeuwen, *J. Exp. Biol.* **207**, 853–868 (2004).

ACKNOWLEDGMENTS

Data reported in the paper are included in the supplementary materials. We thank A. P. Nesmith, M. McKenna, and A. Chandler for discussion on design and K. Hudson and Margherita Gazzola for photography and illustrations. This work was funded by the Harvard Paulson School of Engineering and Applied Sciences, the Wyss Institute for Biologically Inspired Engineering, the National Center for Advancing Translational Sciences grant UH3TR000522, subcontract 312659 from Los Almos National Laboratory under prime DTRA contract DE-AC52-06NA25396, the National Science Foundation (NSF) grant EFRI-0938043, NSF Materials Research Science and Engineering Center grant DMR-1420570, Office of Naval Research Multidisciplinary University Research Initiative grant N000141410533, the Swiss National Science Foundation, the MacArthur Foundation, the Radcliffe Institute, the National Research Foundation of Korea grant 2013K1A4A3055268, and the U.S. Army Research Laboratory and Office contract W911NF-12-2-0036. The views and conclusions contained in this Report are those of the authors and should not be interpreted as representing official policies, expressed or implied, of the Army Research Office or Laboratory, the U.S. government, or any other funding agencies. The U.S. government is authorized to reproduce and distribute reprints for government purposes notwithstanding any copyright notation hereon. Portions of this work were performed at the Harvard Center for Nanoscale Systems (NSF 1541959) and at the Neurobiology Imaging Facility (NINDS P30 Core Center NS072030). Certain aspects of the paper are described in U.S. patent 8,492,150 and U.S. patent application 20150182679.

SUPPLEMENTARY MATERIALS

www.sciencemag.org/content/353/6295/158/suppl/DC1
Materials and Methods
Supplementary Text
Figs. S1 to S15
References (*33*–*44*)
Movies S1 to S20

6 February 2016; accepted 19 May 2016
10.1126/science.aaf4292

Editor's Summary

Swim into the light

A bio-inspired swimming robot that mimics a ray fish can be guided by light. Park *et al*. built a 1/10th-scale version of a ray fish with a microfabricated gold skeleton and a rubber body powered by rat heart muscle cells. The cardiomyocytes were genetically engineered to respond to light cues, so that the undulatory movements propelling the robot through water would follow a light source.

Science, this issue p. 158